Bio-Design and Manufacturing (2021) 4:157–170
https://doi.org/10.1007/s42242-020-00121-4

RESEARCH ARTICLE

3D human nonalcoholic hepatic steatosis and fibrosis models

Sushila Maharjan[1] · Diana Bonilla[1] · Princy Sindurakar[1,2] · Hongbin Li[1] · Wanlu Li[1] · Sergio Duarte[3] · Ali Zarrinpar[3,4,5] · Y. Shrike Zhang[1]

Received: 20 October 2020 / Accepted: 15 December 2020 / Published online: 8 February 2021

Abstract

This study presents a simple and robust three-dimensional human hepatic tissue model to emulate steatotic and fibrotic conditions and provide an in vitro model for drug testing and mechanistic studies. Using a photolithographic biofabrication method with a photomask featuring hexagonal units, liver cells, including a human hepatic cell line (HepG2-C3A) and a human hepatic stellate cell line (LX-2) were embedded in gelatin methacryloyl hydrogel. Hepatic steatosis was induced by supraphysiological concentration of free fatty acids; hepatic fibrosis was induced by transforming growth factor-β1. Induction of steatosis was confirmed by Oil Red O and BODIPY staining and was inhibited with toyocamycin and obeticholic acid. Induction of fibrosis was confirmed by immunostaining for collagen type I and alpha smooth muscle actin and inhibited by rapamycin and curcumin treatment. This model was further preliminarily validated using primary human hepatocytes in a similar setup. These constructs provide a viable, biologically relevant, and higher throughput model of hepatic steatosis and fibrosis and may facilitate the study of the mechanisms of disease and testing of liver-directed drugs.

Keywords Nonalcoholic fatty liver disease (NAFLD) · Gelatin methacryloyl (GelMA) · Photocrosslinking · Steatosis · Fibrosis · Free fatty acids · Transforming growth factor-β1 (TGF-β1)

Introduction

Nonalcoholic fatty liver disease (NAFLD) is one of the most common liver diseases affecting 25% of the global population [1]. NAFLD represents a wide range of liver diseases caused by the excess fat accumulation in hepatocytes in the liver. It includes simple hepatic steatosis without inflammation and nonalcoholic steatohepatitis (NASH) that can further progress to fibrosis, cirrhosis, and hepatocellular carcinoma [2]. Steatosis is marked by the presence of excess fat within the cytoplasm of hepatocytes, i.e., liver fat level more than 5% of the liver weight [3]. Similarly, NASH represents hepatic steatosis in conjunction with liver inflammation and injury. NASH can include fibrosis characterized by the deposition of type I collagen [4]. NASH is associated with obesity, type 2 diabetes, glucose intolerance, and cardiovascular diseases [5–7].

Hepatic steatosis usually occurs as a result of an imbalance in fatty acid metabolism, i.e., an imbalance between fatty acid uptake, synthesis, and catabolism. This results in the formation of intracellular fat droplets [8], ultimately leading to portal and lobular inflammation and hepatic injury [9]. Approximately 20% of patients with hepatic steatosis

Electronic supplementary material The online version of this article (https://doi.org/10.1007/s42242-020-00121-4) contains supplementary material, which is available to authorized users.

✉ Ali Zarrinpar
ali.zarrinpar@surgery.ufl.edu

✉ Y. Shrike Zhang
yszhang@research.bwh.harvard.edu

1 Division of Engineering in Medicine, Department of Medicine, Brigham and Women's Hospital, Harvard Medical School, 65 Landsdowne St, Cambridge, MA 02139, USA

2 Department of Biology, College of the Holy Cross, Worcester, MA 01610, USA

3 Department of Surgery, University of Florida, 1600 SW Archer Rd, Gainesville, FL 32610, USA

4 Department of Biomedical Engineering, University of Florida, Gainesville, FL 32610, USA

5 Department of Biochemistry and Molecular Biology, University of Florida, Gainesville, FL 32610, USA

have been found to have hepatic inflammation characterized by infiltration of inflammatory cells including macrophages, dendritic cells, and T lymphocytes [9]. Accumulation of fat in liver also leads to the development of insulin resistance [10]. Due to these events, steatosis can result in hepatic inflammation and fibrosis via hepatic stellate cell activation. Cirrhosis and hepatocellular carcinoma are the most common causes of NASH-associated morbidity and mortality [11]. NASH-associated hepatocellular carcinoma can also occur in the absence of cirrhosis [12]. Although studies have suggested that hepatic fat accumulation is essential for the development of NASH, the molecular mechanisms underlying NASH initiation and progression have not been fully elucidated yet.

Understanding the molecular mechanisms underlying the physiopathology of NAFLD has mostly been undertaken through animal studies using genetic models or diet-induced models, which were later corroborated by clinical studies [13]. Despite the intensive investigation of therapeutic regimens for NAFLD, there is no drug currently FDA approved for the treatment for NASH [14]. This has been attributed partly to the lack of reliable high(er)-throughput liver disease models. Recently, in vitro approaches have been explored to study the progression of NAFLD. However, few in vitro NAFLD models have been developed. Generally, immortalized cell lines are widely used to develop in vitro models for research. Most current models for NAFLD, including in vitro cell and animal models, fail to recapitulate human liver pathophysiological models due to inappropriate cellular compositions and inducers used for the disease modeling [15, 16].

During the past decade, several scaffold-free and scaffold-based in vitro models have been developed to study fatty liver disease, including microfluidic liver-on-a-chip devices, hepatic sandwich culture models, and three-dimensional (3D) hepatic spheroids [17–23]. For example, 3D-bioprinted human liver tissue constructs, comprised of human hepatocytes, hepatic stellate cells (HSCs), and endothelial cells (ECs), were utilized to study transforming growth factor-β1 (TGF-β1)-, methotrexate (MTX)-, and thioacetamide-induced fibrosis [24]. They further modified this liver tissue model by adding Kupffer cells (KCs) and studied the role of KCs in TGF-β1- and MTX-mediated fibrogenesis [25].

However, limitations of most of these in vitro liver models include insufficient liver architecture, suboptimal cellular phenotypes, limited experimental longevity or scalability, or/and inappropriate disease-inducers. Thus, there remains a need for better in vitro liver models that could recapitulate the in vivo pathophysiology of human NAFLD. 3D biofabrication technologies have been emerging as a promising strategy for the fabrication of tissues in vitro that could serve as tissue models for high(er)-throughput in vitro studies, implants for in vivo studies, or to replace diseased tissues [26]. Photolithographic biofabrication methods use either photomask-based photolithography or maskless photolithography enabling the precise positioning of cell-embedded bioink in a predefined pattern to closely mimic the architecture of real tissue or organ [27–29]. Photomask-based photolithography involves UV exposure of a light-sensitive bioink through the photoresist mask wherein the regions of the bioink solution exposed to light are cured resulting in 3D scaffolds according to the geometric pattern of the photomask used [30]. The most common bioink formulations include hydrogel precursors due to their biocompatibility, porosity, mechanical properties, and resemblance to the native extracellular matrix (ECM) [31]. The photolithographic method has been employed to fabricate 3D tissue scaffolds using various cell types, including hepatocytes [32], NIH 3T3-fibroblasts, C2C12 myoblasts, human hepatocellular carcinoma cells (HepG2), human umbilical vein ECs (HUVECs) [33], HT1080 fibrosarcoma cells [34], and mouse embryonic stem cells [35]. For example, the digital light processing (DLP)-based 3D bioprinting method was used to develop 3D hepatic models wherein human-induced pluripotent stem cell-derived hepatic progenitor cells (hiPSC-HPCs), HUVECs, and adipose-derived stem cells (ADSCs) were patterned in a liver lobule-like structure, and hiPSC-HPCs maturation and functional preservation within 3D liver tissue structures were investigated [28].

Here, we report the development of a 3D human NAFLD models utilizing a simple yet robust photopatterning-based biofabrication approach. We demonstrated the accumulation of fat by hepatocytes within 3D hepatic tissue constructs after exposure to free fatty acids. The 3D hepatic tissues further exhibited enhanced type I collagen deposition by the HSCs after TGF-β1 treatment. Moreover, the free fatty acid-induced steatotic tissues and TGF-β1-induced fibrotic tissues were successfully treated with antisteatotic and antifibrotic drugs, respectively. Taken together, these in vitro 3D-biofabricated NAFLD models could provide a platform to study pathogenesis of steatosis and fibrosis, as well as serve as an accurate NAFLD model for drug screening.

Materials and methods

Gelatin from porcine skin (type-A, 300 bloom), methacrylic anhydride, calcium chloride ($CaCl_2$), 2-hydroxy-4′-(2-hydroxyethoxy)-2-methylpropiophenone (Irgacure 2959), Triton X-100, bovine serum albumin (BSA), urea assay kit, oleic acid, palmitic acid, isopropyl alcohol, obeticholic acid, toyocamycin, rapamycin (sirolimus) solution, curcumin, and Oil Red O were purchased from Sigma-Aldrich (MO, USA). Dulbecco's modified Eagle medium (DMEM), Dulbecco's phosphate-buffered saline (DPBS), fetal bovine serum (FBS), trypsin-ethylenediaminetetraacetic acid

(trypsin–EDTA), penicillin/streptomycin (P/S), antibiotic–antimycotic solution stabilized (Anti–Anti, 100×), 4′,6-diamidino-2-phenylindole (DAPI), formalin (10% w/v), Live/Dead® Viability/Cytotoxicity Kit, Alexa Fluor® 594-phalloidin, BODIPY™ 493/503, CM-DiI dye, green CMFDA (5-chloromethylfluorescein diacetate) dye, blue CMAC (7-amino-4-chloromethylcoumarin) dye, and dialysis membrane (M_w cutoff: 12,000-14,000 Da) were obtained from Thermo Fisher Scientific (MA, USA). Stellate cell medium and stellate cell growth supplements were acquired from ScienCell (CA, USA). Human albumin ELISA kit, rabbit anticollagen I antibody, rabbit antialpha smooth muscle actin (α-SMA) antibody, and Alexa Fluor® 594-conjugated goat antirabbit secondary antibody were purchased from Abcam (MA, USA). Human TGF-β1 was obtained from PeproTech (NJ, USA). Sylgard 184 silicone elastomer kit for the fabrication of polydimethylsiloxane (PDMS) devices was obtained from Dow Corning (MI, USA). Deckgläser cover glass slides of 15 mm in diameter were obtained from Carolina Biological Supply (NC, USA). Syringe filters (0.22 µm in pore size) were purchased from VWR International (MA, USA). The honeycomb-patterned photomask was obtained CAD/ART Services (Bandon, OR). All other chemicals used in this study were obtained from Sigma-Aldrich unless otherwise mentioned.

Synthesis of gelatin methacryloyl (GelMA)

GelMA was synthesized as described by us previously [36–38]. The synthesis of GelMA was done by the chemical reaction between gelatin and methacrylic anhydride at 50 °C wherein the hydroxyl and amine groups in the amino acids of gelatin were substituted by methacryloyl groups [39]. Briefly, 10 g of type A gelatin from porcine skin was dissolved in 100 mL of DPBS at 60 °C and 8.0 mL of methacrylic anhydride was added to gelatin solution dropwise with continuous stirring. The reaction was carried out at 50 °C for 3 h and then quenched by a fivefold dilution with warm DPBS (40 °C). The product obtained was dialyzed against warm distilled water for 7 days using a dialysis membrane (M_w cutoff 12–14 kDa) to remove the unreacted methacrylic anhydride. The dialyzed solution was then lyophilized to obtain GelMA in the form of a white porous foam. The lyophilized GelMA was stored at room temperature until further use. 0.3% Irgacure 2959 was added for Photocrosslinking of GelMA.

Cells

The human hepatocellular carcinoma cell line variant C3A (HepG2-C3A cells) was obtained from American Type Culture Collection (VA, USA), whereas the human HSC line (LX-2 cells) was obtained from MilliporeSigma (MA, USA). HepG2-C3A cells were cultured in DMEM supplemented with 10% (v/v) FBS and 1% (v/v) P/S or anti–anti, while LX-2 cells were cultured in stellate cell medium (SteCM) supplemented with 1% (v/v) stellate cell growth supplements, 2% (v/v) FBS and 1% (v/v) P/S or anti–anti. The cells were incubated at 37 °C and 5% CO_2 in a 95% humidified cell incubator until 70–80% confluence. The respective culture media were replaced every 3 days.

Fabrication of the 3D human liver tissue model

Approximately 80%-confluent HepG2-C3A cells and LX-2 cells were washed with DPBS (1×) in their respective T75 flasks after removal of the media. Then, 3 mL of trypsin–EDTA solution (1×) was added and incubated at 37 °C in the incubator for 5 min until the cells were detached, followed by the inhibition of trypsin–EDTA with DMEM supplemented with 10% (v/v) FBS. Both HepG2-C3A cells and LX-2 cells were collected into 15-mL falcon tubes separately, centrifuged at 1000 rpm for 5 min at room temperature and were resuspended in fresh DMEM and SteCM, respectively.

The 10% (w/v) GelMA hydrogel precursor solution containing 0.6% (w/v) Irgacure 2959 was prepared by dissolving GelMA and Irgacure 2959 powder in DPBS at 50 °C and sterilized by filtration through a sterile 0.22-µm syringe filter. The sterilized GelMA precursor solution was kept at 37 °C in an incubator and protected from light until use.

Both HepG2-C3A cells and LX-2 cells were washed twice with DPBS (1×) and resuspended in DPBS before adding to the GelMA precursor solution. Immediately prior to the fabrication of the hepatic tissue constructs, the HepG2-C3A cell suspension was mixed with the 10% (w/v) GelMA hydrogel precursor solution, at a 1:1 ratio, to obtain 5% GelMA hydrogel precursor with 3×10^6 cells/mL. Similarly, the heterogeneous cell suspension, containing 2.5×10^6 cells/mL of HepG2-C3A cells and 1×10^6 cells/mL of LX-2 cells, was added to 10% (w/v) GelMA hydrogel precursor solution (1:1) to obtain 5% GelMA with 3.5×10^6 cells/mL.

Subsequently, 70 µL of the GelMA precursor solution was placed in a circular PDMS mold with 50 µm depth and 12 mm diameter and was covered with a piece of circular cover glass. On top of the circular cover glass slide, the photomask, having hexagonal units resembling the human liver lobule, was placed and exposed under UV light of 0.5 W/cm^2 (OmniCure S2000 Spot UV Curing System) for 30 s to obtain the 3D lobular human liver tissue construct. The cover glass with the photopatterned liver tissue construct was transferred into a well of a 24-well plate and washed with DPBS (1×) to remove uncross-linked GelMA precursor from the construct; 400 µL/well of cell-specific medium was added into each well, and tissue constructs were incubated at 37 °C and 5% CO_2 in a 95%-humidified cell incubator

for downstream experimental analyses. HepG2-C3A constructs were incubated in DMEM supplemented with 10% (v/v) FBS and 1% (v/v) P/S or anti–anti, whereas HepG2-C3A + LX-2 constructs were incubated in common medium containing 1:1 ratio of the DMEM complete medium and the SteCM complete medium. To visualize the localization of HepG2-C3A cells and LX-2 cells within the constructs, HepG2-C3A cells were labeled with the green (CMFDA) or blue (CMAC) cell tracker and LX-2 cells were labeled with red cell tracker (CM-DiI) before tissue fabrication, when necessary.

Cell viability assay

The Live/Dead® Viability/Cytotoxicity Kit was utilized to evaluate cell viability according to manufacturer's instructions. Briefly, the 3D human liver tissue constructs were washed three times with DPBS and incubated with 100 μL/well of the combined Live/Dead assay reagents [2 μM of calcein AM and 4 μM of ethidium homodimer I (EthD-1)] for 20 min at 37 °C in 5% CO_2. The cells were then washed with DPBS and observed under an Axio Observer inverted fluorescence microscope (Zeiss, NY, USA). Percentages of viable cells were determined by using the Image J software (National Institutes of Health, MD, USA).

Induction of steatosis

The 3D human liver tissue constructs were exposed to their specific physiological media supplemented with free fatty acids at day 4 of fabrication; 80 mM each of palmitic acid and oleic acid was prepared in 100% isopropanol. A combination of the saturated palmitic acid (200 μM) and unsaturated oleic acid (200 μM) was used at a 1:1 ratio to resemble human plasma concentrations of free fatty acids. The scaffolds were exposed to free fatty acids for 24 h at 37 °C and 5% CO_2 in a 95%-humidified cell incubator for downstream studies.

Oil Red O and BODIPY staining

Free fatty acid uptake and accumulation in the liver tissue constructs were assessed by Oil Red O staining and BODIPY 493/503 staining according to manufacturer's instructions. For Oil Red O staining, the liver tissue constructs exposed to free fatty acids were washed three times with DPBS (1×) and fixed with 10% formalin for 30 min at room temperature. The scaffolds were washed twice with distilled water, treated with 60% isopropanol for 5 min, and then stained with Oil Red O solution (0.3% in 60% isopropanol) for 20 min at room temperature. After washing five times with distilled water, the constructs were observed and imaged under a fluorescence microscope.

To extract Oil Red O, 400 μL/well of 100% isopropanol was added to the tissue scaffolds and incubated at room temperature for 10 min with gentle shaking on an orbital shaker. Hundred microliters of the Oil Red O extract was transferred to 96-well plate in triplicates, and absorption was measured at 492 nm on a microplate reader (Tecan, Salzburg, Austria).

Similarly, 5 mM of the BODIPY staining stock solution was prepared by dissolving 1.3 mg of BODIPY 493/503 in 1 mL of anhydrous dimethyl sulfoxide (DMSO); 2 μM of BODIPY staining solution was then prepared by 1:2500 dilution in DPBS (1×). The liver tissue constructs exposed to free fatty acids were overlaid with 400 μL/well of the BODIPY staining solution after washing three times with DPBS (1×) and incubated for 5 min at room temperature. The constructs were then washed three times with DPBS (1×) and imaged under a fluorescence microscope.

Antisteatotic drug treatment

Toyocamycin and obeticholic acid were used as antisteatotic drugs. Stock solutions of both of these drugs were prepared in DMSO. The free fatty acid-induced steatotic liver tissue constructs were treated with 0, 10, and 20 μM of the drugs separately and prepared by diluting stock solutions in construct-specific media. The constructs were incubated at 37 °C and 5% CO_2 in a 95%-humidified cell incubator. After 48 h of incubation, the media were assessed for albumin and urea measurements, while the tissue constructs were stained with Oil Red O and BODIPY 493/503 as described above.

Induction of fibrosis

10 μg/mL of the TGF-β1 stock solution was prepared in DPBS (1×). To induce fibrosis, the 3D human liver tissue constructs were exposed to construct-specific media containing 25 ng/mL of TGF-β1 at day 4 of fabrication and incubated for 24 h at 37 °C and 5% CO_2 in a 95%-humidified incubator for further studies.

Immunocytochemical analyses

The TGF-β1-induced fibrotic liver tissue constructs were washed with DPBS and fixed with 10% formalin for 30 min at room temperature. The constructs were washed with DPBS and incubated with the permeabilization buffer (0.1% (v/v) Triton X-100 in DPBS] for 1 h. The constructs were then blocked with 5% (w/v) goat serum in DPBS for 2 h at room temperature and incubated with anticollagen I antibody or antialpha smooth muscle actin (α-SMA) antibody (1:200 dilution) overnight at 4 °C. The samples were washed with DPBS and incubated with the Alexa Fluor® 594-conjugated goat antirabbit secondary antibody (1:200 dilution)

overnight at 4 °C. Finally, the nuclei were counterstained with DAPI after washing with DPBS and examined under a fluorescence microscope.

Antifibrotic drug treatment

Rapamycin and curcumin were used as antifibrotic drugs. 1.0 mg/mL of rapamycin was dissolved in acetonitrile. 1 mg/mL of the curcumin solution was prepared in DMSO. The TGF-β1-induced fibrotic liver tissue constructs were treated with 0, 10, and 20 nM of the drugs separately, prepared by diluting stock solutions in construct-specific media. The constructs were incubated at 37 °C and 5% CO_2 in a 95%-humidified incubator for 48 h. After incubation, the media were collected for albumin and urea measurements, while the tissue scaffolds were immunostained with anticollagen I antibody or antialpha smooth muscle actin (α-SMA) antibody as described above.

Analyses of albumin and urea productions

Albumin secreted by the liver cells within the constructs was measured using the albumin ELISA kit according to the manufacturer's protocol. Briefly, all the reagents were brought to room temperature before starting the assay. Fifty microliters of the standard or sample was added to each well of albumin ELISA plate and incubated for 1 h at room temperature. Each well was then washed three times with 200 µL of the wash buffer (1×). Fifty microliters of the biotinylated albumin antibody was added to each well and incubated for 30 min. Each well was washed again three times with 200 µL of the wash buffer (1×), and 50 µL of the 1× SP conjugate was added to each well. After incubation for 30 min, followed by washing, 50 µL of the chromogen substrate was added per well and incubated for 20 min. Finally, 50 µL of the stop solution was added to each well and the absorbance was read at 450 nm on a microplate reader.

Similarly, urea produced by the liver cells within the constructs was measured using a urea assay kit, according to the manufacturer's instructions. Briefly, 0, 1, 2, 3, 4, and 5 nmol of urea standards were prepared by diluting 100 nmol/mL of the urea standard solution with the urea assay buffer. Fifty microliters of the standard or sample was added to each well of a flat-bottom 96-well plate. Then, 50 µL of the freshly prepared reaction mix was added to each well and mixed quickly by gently rocking the plate. The plate was incubated at 37 °C for 1 h and absorbance was measured at 570 nm on the microplate reader.

Statistical analyses

All experiments were done in three technical replicates, and the results were presented as means ± standard deviations. Statistical analyses were performed by pairwise *t* test using GraphPad Prism Software (CA, USA), and $p \le 0.05$ was considered as statistically significant ($*p \le 0.05$, $**p \le 0.01$, $***p \le 0.001$).

Results

The 3D lobular hepatic tissue model

The 3D hepatic tissue model was generated by a photolithographic biofabrication method using a photomask featuring hexagonal units (Fig. S1), and hepatic cells [a human hepatocellular carcinoma cell line (HepG2-C3A cells) and a human HSC line (LX-2 cells)] embedded in 5% (w/v) GelMA (Fig. 1a). HepG2-C3A and LX-2 cells are widely used as model cells for the fabrication of engineered in vitro liver tissues including NASH models [40–42]. The liver is generally comprised of approximately 60–70% of hepatocytes and 30–40% of nonparenchymal cells [43]. Since stellate cells are best known for their critical role in fibrosis [44], LX-2 HSCs were chosen as the nonparenchymal cell population in the study. Further, the HepG2-C3A and LX-2 cell ratio was chosen to give the close resemblance of the cellular distribution in native liver, approximately 70% hepatocytes and 30% nonparenchymal cells [45, 46].

GelMA has been widely used to fabricate in vitro tissue scaffolds due to its physicochemical properties, biodegradability, photocross-linking ability, and tunable mechanical properties [47–49]. GelMA is obtained by the methacryloyl modification of gelatin, a hydrolytic product of collagen that is the main component of the native ECM. GelMA features arginine–glutamine–aspartic acid (RGD) sequences that promote cell adhesion and proliferation [50]. Matrix stiffness of photopolymerized 5% (w/v) GelMA has been found to be similar to the native liver tissue [28]. Therefore, liver tissue constructs with native liver tissue-like matrix stiffness were fabricated using 5% (w/v) GelMA that supported the proliferation and growth of hepatic cells.

The 3D human liver tissue constructs of approximately 5 mm in size and 500 µm in thickness were comprised of hexagonal lobules arranged in a honeycomb-like configuration, resembling the native liver lobules (Fig. 1b). These constructs containing HepG2-C3A cells and LX-2 cells (hereafter referred to as HLT-2 constructs) were cultured in the coculture medium prepared by mixing 1:1 ratio of DMEM complete medium and SteCM complete medium at 37 °C and 5% CO_2 in a 95%-humidified incubator for downstream studies at designated times. The hepatic tissue constructs prepared with only HepG2-C3A cells (hereafter referred to as HLT-1 constructs) were used as controls (Fig. S2). The viability of cells within the hepatic tissue constructs was found to increase gradually with culture

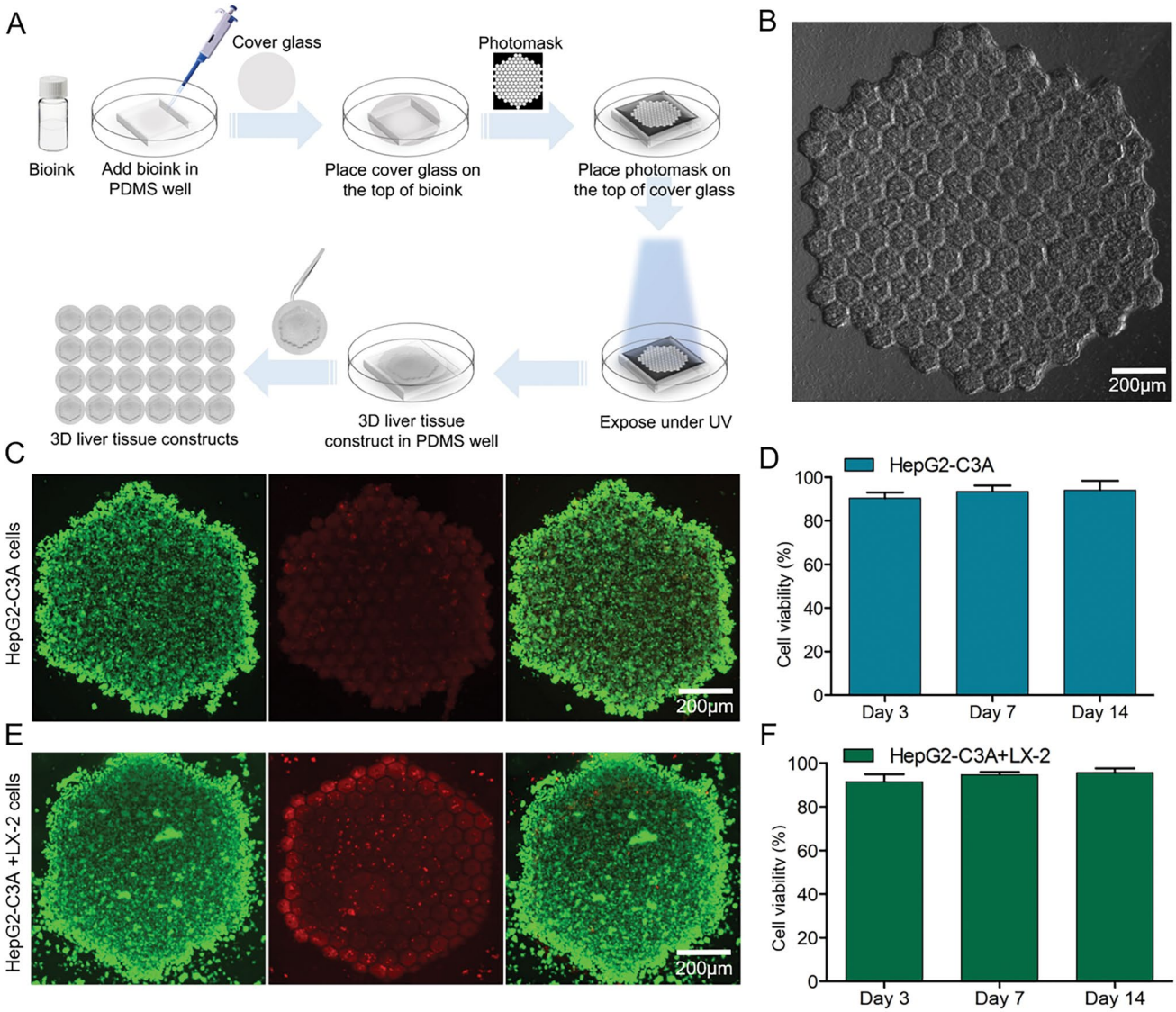

Fig. 1 Fabrication of the 3D hepatic tissue model. **a** Schematics showing the steps involved in the fabrication of the 3D hepatic tissue model. **b** Bright-field image of a 3D hepatic model. **c** Viability of HepG2-C3A cells within the 3D hepatic tissue model (HLT-1) at day 7. **d** Viability of HepG2-C3A cells within HLT-1 constructs at various time points. **e** Viability of cocultured HepG2-C3A and LX-2 cells within the 3D hepatic tissue model (HLT-2) at day 7. **f** Viability of cocultured HepG2-C3A and LX-2 cells within HLT-2 constructs at different time points

time and reached more than 90% at day 14 for both HLT-1 (Fig. 1c, d) and HLT-2 (Fig. 1e, f) constructs. Even though these cells were initially mixed during fabrication, interestingly, HepG2-C3A and LX-2 cells within the liver tissue constructs demonstrated their intrinsic behaviors. Over a period of 7 days in culture, HepG2-C3A cells remained within the lobules, whereas LX-2 cells were found to proliferate and migrate toward the peripheries of the lobular units to reside in the perisinusoidal-like spaces between the lobules (Fig. 2), exhibiting the typical characteristics of HSCs in the liver. The migration and localization of HepG2-C3A cells and LX-2 cells within the liver tissue constructs were monitored by labeling the HepG2-C3A and LX-2 cells with blue (CMAC) and red (CM-DiI) cell trackers, respectively, over the period of 7 days (Fig. 2a–c). The localizations of HepG2-C3A cells and LX-2 cells within the liver tissue constructs were also clearly visible wherein spherical-shaped HepG2-C3A cells were located within the lobules and spindle-shaped LX-2 cells resided along the peripheries of the hexagonal lobules forming the hexagonal network in the perisinusoidal-like spaces between the lobules (Fig. 2d). In their native state, HSCs are located in the perisinusoidal space of the liver so as to

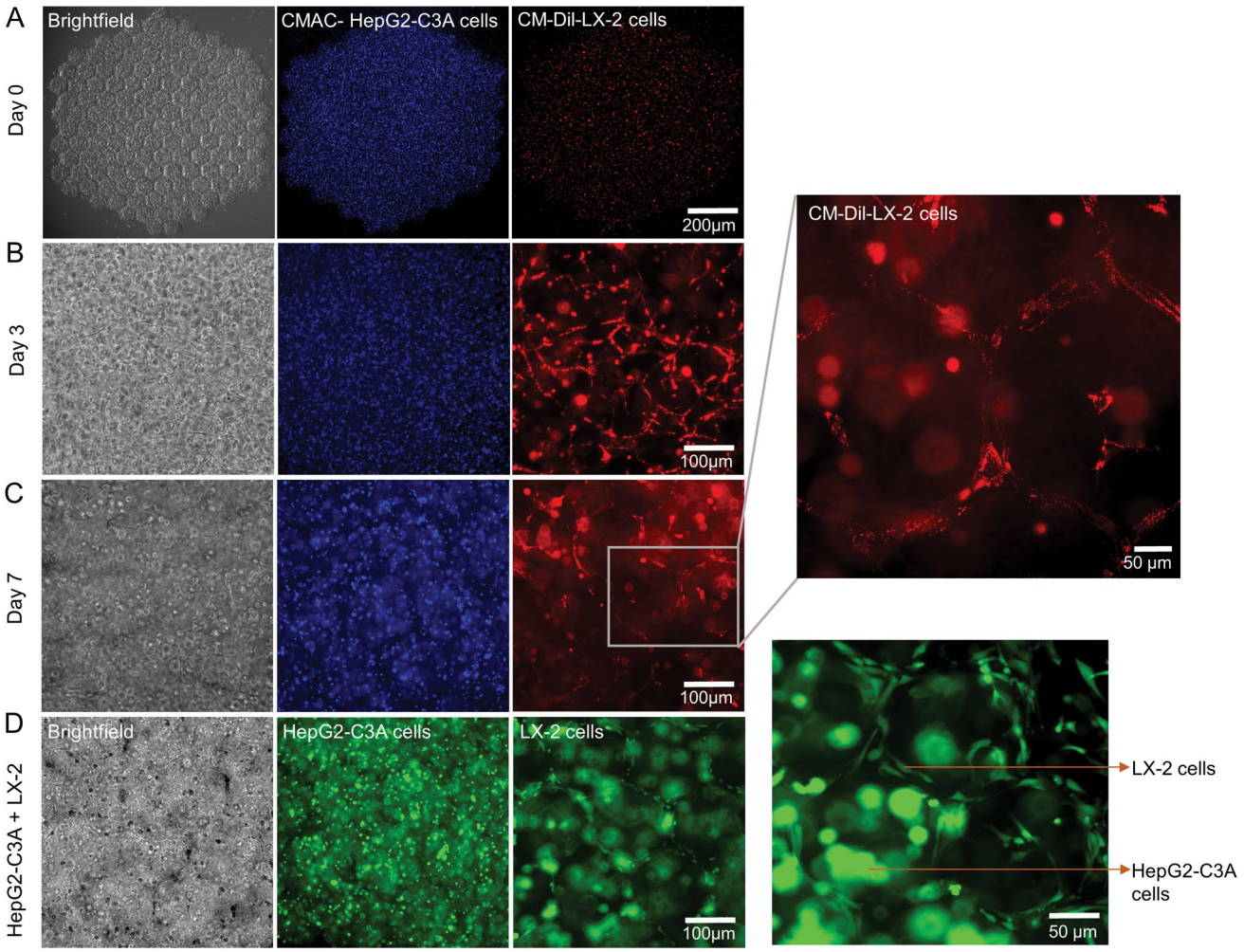

Fig. 2 Orientation of HSCs. **a** Fluorescence images of HepG2-C3A cells (labeled with blue cell tracker) and LX-2 cells (labeled with red cell tracker) within HLT-2 constructs at day 0. **b** Fluorescence images of HepG2-C3A cells and LX-2 cells within the HLT-2 construct at day 3, showing the spreading of LX-2 cells. **c** Fluorescence images of HepG2-C3A cells and LX-2 cells within the HLT-2 construct at day 7, showing the distributions of HepG2-C3A cells within the lobules and LX-2 cells along the peripheries of the hexagonal lobules. **d** Fluorescence images showing the calcein AM-stained viable HepG2-C3A cells within the lobules and LX-2 cells along the peripheries of the hexagonal lobules at day 7, followed by higher magnification image clearly showing LX-2 cells forming the hexagonal network within the HLT-2 construct

interact with hepatocytes, sinusoidal endothelial cells, and other hepatic cells [51].

The 3D NASH model

Palmitic acid and oleic acid were used to induce steatosis in the 3D hepatic tissue constructs. Initially, we investigated different concentrations of the palmitic acid (100–400 μM) and oleic acid (100–400 μM), individually or in combination (1:1 ratio) for different time periods (24 h and 48 h) to develop the in vitro NASH model. The induction of steatosis was found to be dependent on the dose of free fatty acids used. On the basis of preliminary observations, the HLT-1 and HLT-2 constructs were exposed with the combination of oleic acid (200 μM) and palmitic acid (200 μM) at a 1:1 ratio for 24 h for induction of steatosis, leading to development of the in vitro NASH model under given experimental conditions. Free fatty acid uptake and accumulation in liver cells within the constructs were observed by Oil Red O staining of fatty acids (Fig. 3a, b).

We next studied the inhibitory effects of toyocamycin and obeticholic acid on free fatty acid-induced steatosis in our 3D NASH model. After 24 h of free fatty acid exposure, the constructs were treated with toyocamycin (20 μM) and obeticholic acid (20 μM), individually for 48 h. Interestingly, both of these drugs significantly reduced Oil Red O fluorescence in the NASH models, indicating the reduction of accumulated free fatty acids in liver cells within the 3D liver tissue

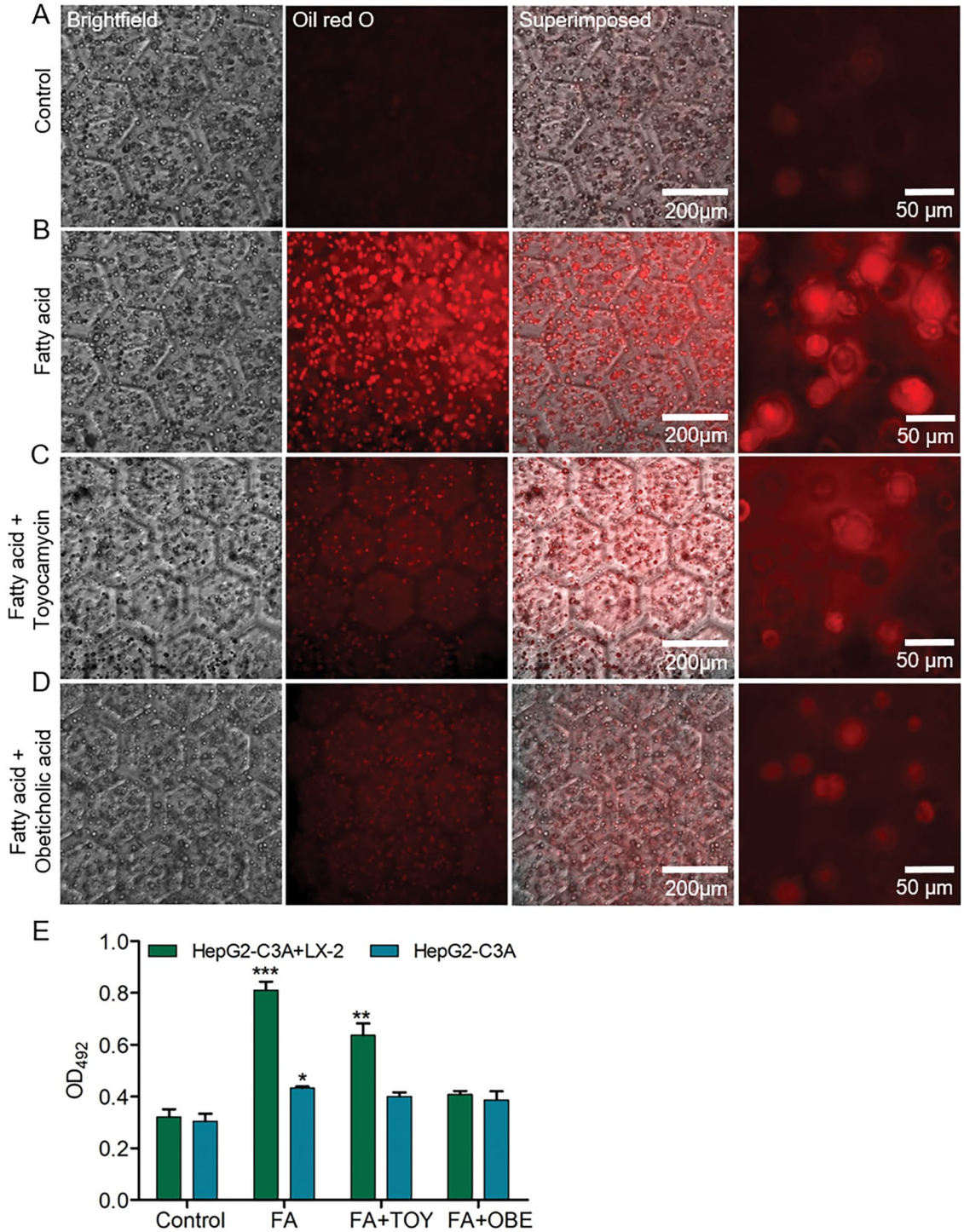

Fig. 3 Free fatty acid accumulation in liver cells. **a** Fluorescence images showing the Oil Red O-stained fatty cells within the HLT-2 construct without free fatty acid treatment. **b** Fluorescence images showing the Oil Red O-stained fatty cells within the HLT-2 construct after incubation with free fatty acids (FA, 200 μM of oleic acid + 200 μM of palmitic acid) for 24 h. **c** Fluorescence images showing the Oil Red O-stained fatty cells within the HLT-2 construct after treatment with toyocamycin (TOY, 20 μM) for 24 h. **d** Fluorescence images showing the Oil Red O-stained fatty cells within the HLT-2 construct after treatment with obeticholic acid (OBE, 20 μM) for 24 h. **e** Quantification of free fatty acids within the HLT-1 and HLT-2 constructs before and after treatment with free fatty acids for 24 h followed by toyocamycin or obeticholic acid for 48 h. Asterisks represent a significant difference between the groups by pairwise *t* tests (*$p \le 0.05$; **$p \le 0.01$; ***$p \le 0.001$, *ns* not significant)

constructs (Fig. 3c, d). The free fatty acids accumulated within the HLT-2 and HLT-1 constructs were significantly lower compared to the untreated constructs. Furthermore, under the given conditions, obeticholic acid was found to be more effective than toyocamycin in reducing the accumulated free fatty acids from the 3D liver constructs. It was also notable that the uptake of free fatty acids, as well as their accumulation in liver cells and removal after drug treatment, was higher in the HLT-2 constructs as compared to those in the HLT-1 constructs (Fig. 3e), indicating the HLT-2 constructs comprising of HepG2-C3A cells and LX-2 cells were comparatively more functional than the HLT-1 constructs, which had only HepG2-C3A cells (Fig. S3). Similar results were obtained when fatty acid accumulation within the constructs was assessed with BODIPY staining. BODIPY-induced fluorescence was reduced significantly in both toyocamycin (20 µM)- and obeticholic acid (20 µM)-treated NASH models as compared to the untreated constructs (Fig. 4a–d).

The functionality of the free fatty acid-induced NASH models was evaluated by measuring the albumin and urea produced by the liver cells within the constructs, before and after drug treatment. Under the normal condition, albumin production by the HLT-2 constructs was significantly higher than the HLT-1 constructs (Fig. 4e), whereas no significant difference was observed in the secretion of urea between the HLT-2 and HLT-1 constructs (Fig. 4f). The cells within the constructs remained viable during the steatotic process and continued to secrete albumin and urea under the pathologic NASH conditions. However, the secretion of albumin was critically reduced in NASH conditions; it recovered by about 40% after treatment of either toyocamycin or obeticholic acid (Fig. 4e). On the other hand, even though the secretion of urea was significantly reduced after free fatty acid exposure, no significant difference in its production was observed after drug treatment (Fig. 4f).

The 3D hepatic fibrosis model

Hepatic fibrosis was induced by exposing the 3D human liver tissue constructs to 25 ng/mL of TGF-β1 as described above. The induction of hepatic fibrosis was confirmed by the immunostaining of collagen type I. Fibrotic constructs exhibited significantly higher production of collagen type I, a typical characteristic of the fibrotic liver, as compared to the normal constructs in both HLT-2 (Fig. 5a) and HLT-1 (Fig. S4A, B). Similarly, during hepatic fibrosis, HSCs become activated by fibrogenic cytokines such as TGF-β1 and transdifferentiate into myofibroblasts that express α-SMA. Therefore, α-SMA is used as a biomarker for activated HSCs in liver fibrosis. The development of TGF-β1-induced fibrotic pathological condition was further confirmed by immunostaining of LX-2 cells with α-SMA (Fig. 5b). The expression of α-SMA was not observed in control constructs.

We also studied the effect of rapamycin and curcumin on TGF-β1-induced fibrotic model. The HLT-2 and HLT-1 constructs were treated with rapamycin (10 nM) and curcumin (10 nM), in separate experiments, after 24 h of TGF-β1 treatment. Both drugs significantly reduced the expression of collagen type I in both HLT-2 (Fig. 5c, d) and HLT-1 (Fig. S4C—E) constructs. However, the expression of collagen type I within HLT-1 constructs was comparably less than that within HLT-2 constructs after TGF-β1 exposure (Figs. 5d, S4E). Similarly, the inhibitory effects of both rapamycin and curcumin on fibrosis were less in HLT-1 constructs when compared to those in HLT-2 constructs as demonstrated by the expression levels of collagen type I in HLT-2 (Fig. 5) and HLT-1 (Fig. S4) constructs.

The functionality of the TGF-β1-induced fibrotic models was evaluated by measuring the albumin and urea productions by the liver cells within the constructs, before and after drug treatment. As in the case of NASH pathologic conditions, the cells within the fibrotic liver constructs secreted albumin and urea under pathologic conditions. Yet, the secretion of albumin was significantly reduced in fibrotic conditions; it recovered by about 20% after treatment of either rapamycin or curcumin (Fig. 5e). On the other hand, no significant differences in the secretions of urea was observed between normal and fibrotic conditions, as well as after drug treatment (Fig. 5f).

Discussions

Here, we present a simple and rapid photolithographic biofabrication of 3D liver tissue constructs that resemble the in vivo-like structure of hepatic lobules comprised of two important cellular types of the liver, hepatocytes and HSCs. While hepatocytes are the major parenchymal cells of the liver that are responsible for metabolic, endocrine, and secretory functions [52], HSCs are pericytes found in the perisinusoidal spaces of the liver [53]. HSCs play an important role in hepatic fibrogenesis and contribute to the accumulation of collagen during chronic liver disease. In the normal liver, HSCs largely exist as inactive nonproliferative cells but become activated by fibrogenic cytokines such as TGF-β1 during chronic liver disease and transdifferentiate into myofibroblasts [53]. Activation of HSCs from quiescent cells into fibrogenic myofibroblasts has been well-established as a driving process of hepatic fibrosis in chronic liver injury. Studies have shown that HSC activation not only is associated with hepatic fibrosis, but also contributes to hepatic steatosis and inflammation [54]. The biofabricated 3D human liver tissue constructs are comprised of hexagonal hepatocyte lobules wherein the LX-2 cells were located in the peripheries of the hexagonal units (Figs. 1, 2), exhibiting the typical characteristics of HSCs in the liver.

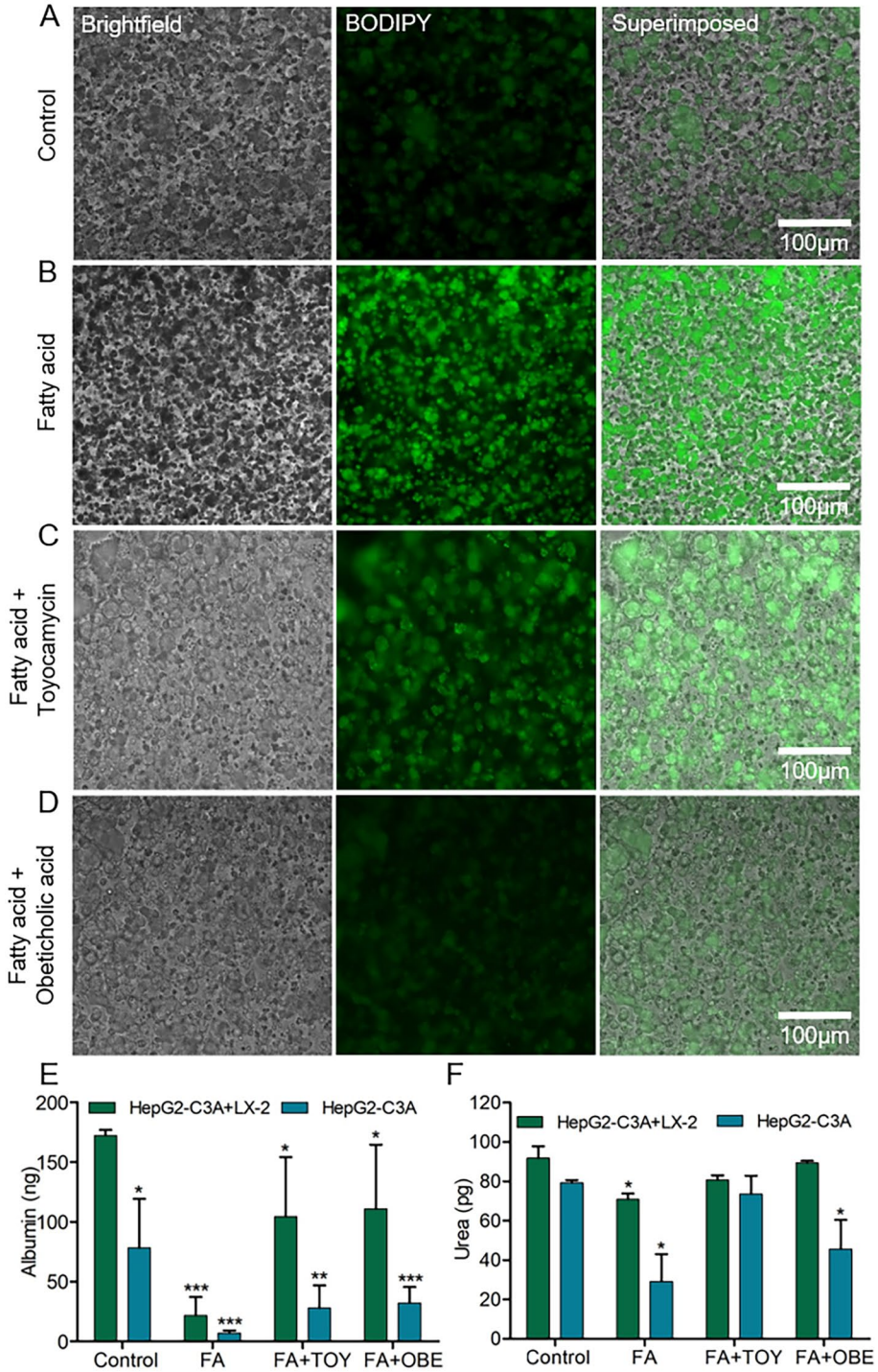

Fig. 4 Effects of free fatty acid accumulation on the liver tissue and treatment. **a** Fluorescence images showing the BODIPY-stained fatty cells within the HLT-2 construct without free fatty acid (FA) treatment. **b** Fluorescence images showing the BODIPY-stained fatty cells within the HLT-2 construct after free fatty acid treatment. **c** Fluorescence images showing the BODIPY-stained fatty cells within the HLT-2 construct after toyocamycin (TOY, 20 μM) treatment for 24 h. **d** Fluorescence images showing the BODIPY-stained fatty cells within the HLT-2 construct after obeticholic acid (OBE, 20 μM) treatment for 24 h. **e** Albumin productions by HepG2-C3A cells within the HLT-1 and HLT-2 constructs before and after 48 h of treatment with TOY or OBE. **f** Urea productions by HepG2-C3A cells within HLT-1 and HLT-2 constructs before and after 48 h of treatment with TOY or OBE. Asterisks represent a significant difference between the groups by pairwise *t* tests (*$p \le 0.05$; **$p \le 0.01$; ***$p \le 0.001$, *ns* not significant)

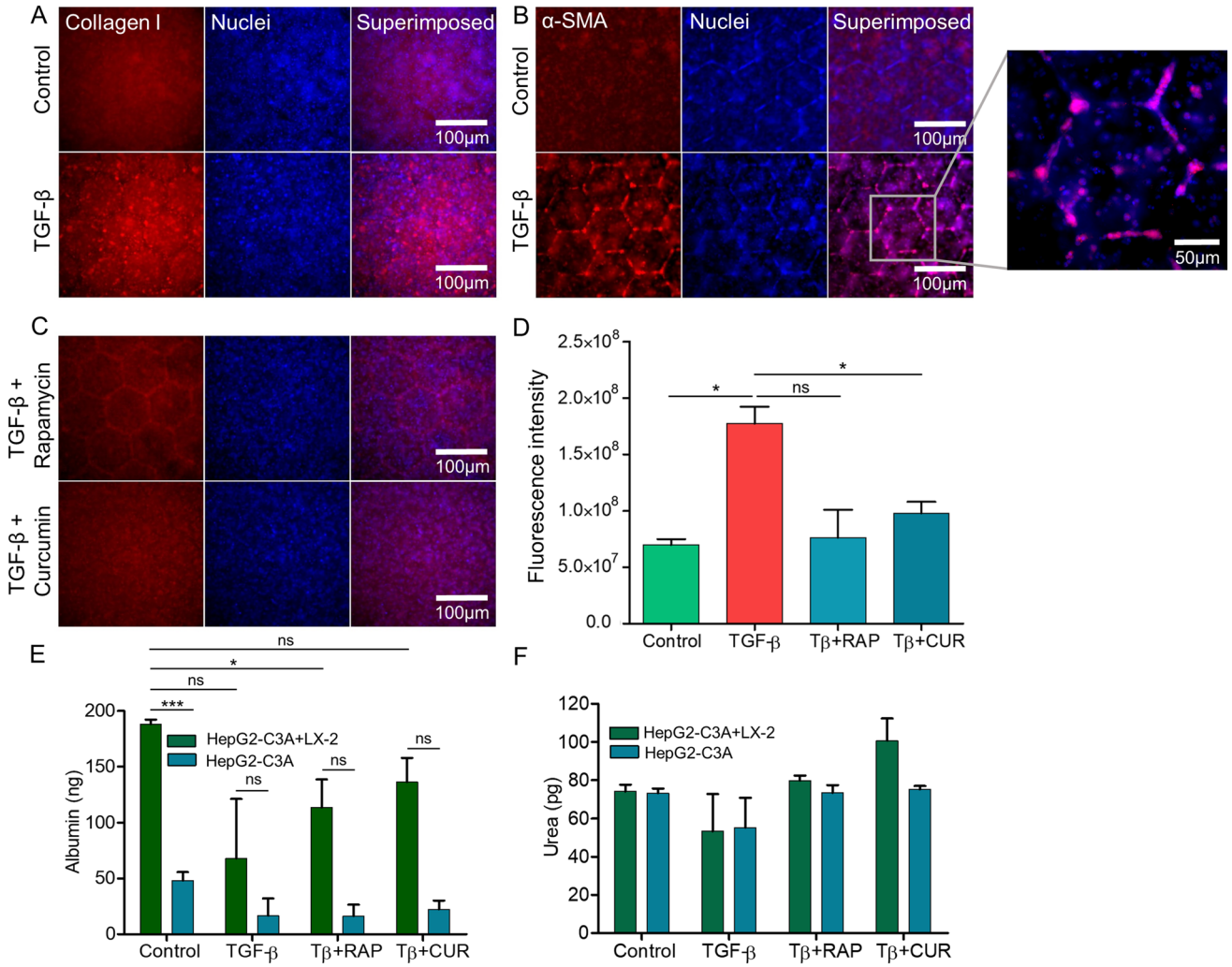

Fig. 5 Induction of fibrosis with TGF-β1 in the 3D liver tissue model and effect of antifibrotic drug treatment. **a** Fluorescence images showing the collagen I and nuclei staining for cells within the HLT-2 constructs without TGF-β1 treatment (upper panel) or after TGF-β1 treatment (25 ng/mL, lower panel) for 24 h. **b** Fluorescence images showing the expression of α-SMA by LX-2 cells within the HLT-2 constructs without TGF-β1 treatment (upper panel) or after TGF-β1 treatment (25 ng/mL, lower panel) for 24 h. **c** Fluorescence images showing the collagen I- and nuclei-stained cells within the HLT-2 constructs after rapamycin (RAP, 10 nM, upper panel) or curcumin (CUR, 10 nM, lower panel) treatment for 48 h. **d** Quantification of collagen I expression by cells within the HLT-2 constructs before and after 48 h of drug treatment. **e** Albumin productions by HepG2-C3A cells within the HLT-1 and HLT-2 constructs before and after 48 h of treatment with rapamycin (RAP, 10 nM) or curcumin (CUR, 10 nM). **f** Urea productions by HepG2-C3A within the HLT-1 and HLT-2 constructs before and after 48 h of treatment with rapamycin (RAP) or curcumin (CUR). Asterisks represent a significant difference between the groups by pairwise *t* tests (*$p \le 0.05$; ***$p \le 0.001$, *ns* not significant)

The biofabricated 3D hepatic tissue model was further utilized to induce two different stages of NAFLD, free fatty acid-induced steatosis and TGF-β1-induced hepatic fibrosis. Different in vitro NAFLD models have been developed in which hepatocytes were treated with monounsaturated and/or saturated free fatty acids, usually palmitic acid or oleic acid or combinations of these two fatty acids [55]. Palmitic acid and oleic acid are the most abundant fatty acids in both normal liver and diseased liver [56]. Therefore, we used palmitic acid and oleic acid for the induction of steatosis in the 3D hepatic tissue constructs. The induction of steatosis was fatty acid dose-dependent and was confirmed by Oil Red O and BODIPY staining for free fatty acids accumulated in the liver cells (Figs. 3, 4). Recently, toyocamycin, an inhibiter of Inositol-requiring enzyme 1-alpha (IRE1α)-X-box binding protein 1 (XBP1) activation, was reported to inhibit free fatty acid-induced steatosis. It was also found to reduce palmitic acid-induced hepatocyte lipoapoptosis in hepatocyte culture [55]. On the other hand, obeticholic acid, a 6a-ethyl derivative of chenodeoxycholic acid, was shown to be useful for the treatment for NASH. Treatment for NASH in a murine

model with obeticholic acid prevented chronic inflammation and liver fibrosis [56]. Consistent with previous studies, the free fatty acids accumulated within the HLT-2 and HLT-1 constructs were significantly reduced by treatment with toyocamycin and obeticholic acid as compared to the untreated constructs. However, obeticholic acid was found to be more effective than toyocamycin in reducing the accumulated free fatty acids within the 3D liver constructs. Further, secretion of albumin was reduced in NASH conditions but recovered by about 40% after treatment of either toyocamycin or obeticholic acid. In contrast, no significant difference in the production of urea was observed after drug treatment, even though its secretion was significantly reduced after free fatty acid treatment (Figs. 3, 4).

Similarly, hepatic fibrosis is a hallmark of chronic liver disease including NASH and is characterized by the excess production of ECM components such as collagens [57]. As a consequence of liver injury, quiescent HSCs get exposed to apoptotic hepatocytes as well as profibrogenic and inflammatory factors, resulting into trans-differentiation of quiescent HSCs into myofibroblasts that are capable of producing excess amounts of ECM components [58]. HSCs represent the major cells that produce ECM proteins, such as collagens, in the injured liver. Among the different profibrogenic cytokines produced by hepatocytes, TGF-β plays a critical role in the development of hepatic fibrosis. Multiple experiments in animal models and human clinical studies have shown increased TGF-β signaling during hepatic fibrosis [59] causing cell damage along with enhanced secretion of profibrogenic and inflammatory cytokines that lead to the apoptosis and hepatic fibrogenesis, as well as carcinogenesis [60]. We induced hepatic fibrosis by exposing the 3D human liver tissue constructs to 25 ng/mL of TGF-β1 and confirmed it by the immunostaining of collagen type I, as well as by immunostaining of LX-2 cells with α-SMA as HSCs transdifferentiate into myofibroblasts in the presence of fibrogenic cytokines such as TGF-β1 (Fig. 5).

Several studies have shown that rapamycin, a bacterial macrolide antibiotic, blocks cell proliferation by inhibiting the G1/S transition of fibroblasts and thus has been used for treating fibrotic diseases [61]. Similarly, recent studies have reported that curcumin, a main component of turmeric, inhibits hepatic fibrosis and cirrhosis via the nuclear factor kappa B (NF-κB) pathway [62], while other studies have shown the anti-inflammatory and antioxidant properties of curcumin [63]. Antifibrotic effects of rapamycin and curcumin were assessed on TGF-β1-induced 3D hepatic fibrotic model and found that these drugs reduced the expression level of collagen type I, indicating the inhibition of TGF-β1-induced fibrosis in a 3D hepatic model. While the secretion of albumin was significantly reduced in fibrotic conditions that was recovered by about 20% after treatment of either rapamycin or curcumin, no significant differences in the secretions of urea were observed under fibrotic and drug-treated conditions (Fig. 5).

In conclusion, the 3D hepatic tissue model presented here has the potential to facilitate the development of models of various liver diseases and testing of liver-directed drugs. The hepatic tissue constructs were fabricated separately, one at a time. It is possible, however, to fabricate these mini-livers concurrently at a much higher throughput [28]. Despite several clinical trials, there are no United States Food and Drug Administration (FDA)-approved drugs for the treatment for NASH and NAFLD [64]. Therefore, improved and physiologically relevant in vitro hepatic disease models are in urgent need to facilitate the study of underlying mechanism of the pathogenesis of the diseases, as well as for rapid prediction of drug responses. A step beyond, we have further demonstrated the feasibility of producing human primary hepatocyte-based 3D hepatic tissue models, where free fatty acid treatment induced lipid accumulation (Fig. S5A). Similarly, TGF-β1 treatment led to fibrosis (Fig. S5B), where additional inclusion of LX-2 HSCs seemed to promote collagen deposition comparing to the monoculture of primary hepatocytes (Fig. S5C).

Author contributions SM, SD, AZ, and YSZ were involved in conceptualization. SM, DB, and PS were involved in data curation. SM, DB, and YSZ performed formal analysis. SM, DB, PS, HL, WL, AZ, and YSZ conducted investigation. SM, DB, SD, and YSZ contributed to methodology. AZ and YSZ contributed to project administration. AZ and YSZ contributed resources. AZ and YSZ conducted supervision. SM, AZ, and YSZ were involved in validation. SM and YSZ contributed to visualization. SM, AZ, and YSZ were involved in writing original draft. SM, DB, PS, HL, WL, SD, AZ, and YSZ were involved in writing review and editing.

Funding YSZ received funding from National Institutes of Health (K99CA201603, R00CA201603, R21EB025270, R21EB026175, R01EB028143, R03EB027984), National Science Foundation (1935105), Brigham Research Institute New England Anti-Vivisection Foundation, and American Fund for Alternatives to Animal Research (AFAAR). AZ received funding from National Institutes of Health (K08DK113244, R01MD012579). SD received funding from National Institutes of Health (R01MD012579-UT20664DS).

Availability of data and materials The datasets that support the findings of this study are available from the corresponding authors upon reasonable request. All requests for raw and analyzed data and materials will be promptly reviewed by the Brigham and Women's Hospital and University of Florida to verify whether the request is subject to any intellectual property or confidentiality obligations. Any data and materials that can be shared will be released via a Material Transfer Agreement.

Compliance with ethical standards

Ethical approval This article does not contain any studies with human or animal subjects performed by any of the authors.

Conflict of interest The authors have no relevant conflicts of interest to declare.

Consent to participate Consent to participate is not applicable in this study.

References

1. Wang XJ, Malhi H (2018) Nonalcoholic fatty liver disease. Ann Intern Med 169(9):itc65–itc80. https://doi.org/10.7326/AITC201811060
2. Friedman SL, Neuschwander-Tetri BA, Rinella M et al (2018) Mechanisms of NAFLD development and therapeutic strategies. Nat Med 24(7):908–922. https://doi.org/10.1038/s41591-018-0104-9
3. Chalasani N, Younossi Z, Lavine JE et al (2018) The diagnosis and management of nonalcoholic fatty liver disease: practice guidance from the American Association for the Study of Liver Diseases. Hepatology 67(1):328–357. https://doi.org/10.1002/hep.29367
4. Vuppalanchi R, Chalasani N (2009) Nonalcoholic fatty liver disease and nonalcoholic steatohepatitis: selected practical issues in their evaluation and management. Hepatology 49(1):306–317. https://doi.org/10.1002/hep.22603
5. Marchisello S, Di Pino A, Scicali R et al (2019) Pathophysiological, molecular and therapeutic issues of nonalcoholic fatty liver disease: an overview. Int J Mol Sci 20(8):1948. https://doi.org/10.3390/ijms20081948
6. Lonardo A, Sookoian S, Chonchol M et al (2013) Cardiovascular and systemic risk in nonalcoholic fatty liver disease—atherosclerosis as a major player in the natural course of NAFLD. Curr Pharm Des 19(29):5177–5192. https://doi.org/10.2174/1381612811319290003
7. Gastaldelli A, Cusi K (2019) From NASH to diabetes and from diabetes to NASH: mechanisms and treatment options. JHEP Rep Innov Hepatol 1(4):312–328. https://doi.org/10.1016/j.jhepr.2019.07.002
8. Gluchowski NL, Becuwe M, Walther TC et al (2017) Lipid droplets and liver disease: from basic biology to clinical implications. Nat Rev Gastroenterol Hepatol 14(6):343–355. https://doi.org/10.1038/nrgastro.2017.32
9. Koyama Y, Brenner DA (2017) Liver inflammation and fibrosis. J Clin Invest 127(1):55–64. https://doi.org/10.1172/JCI88881
10. Samuel VT, Shulman GI (2016) The pathogenesis of insulin resistance: integrating signaling pathways and substrate flux. J Clin Invest 126(1):12–22. https://doi.org/10.1172/JCI77812
11. Ekstedt M, Hagström H, Nasr P et al (2015) Fibrosis stage is the strongest predictor for disease-specific mortality in NAFLD after up to 33 years of follow-up. Hepatology 61(5):1547–1554. https://doi.org/10.1002/hep.27368
12. Baffy G, Brunt EM, Caldwell SH (2012) Hepatocellular carcinoma in non-alcoholic fatty liver disease: an emerging menace. J Hepatol 56(6):1384–1391. https://doi.org/10.1016/j.jhep.2011.10.027
13. Schattenberg JM, Galle PR (2010) Animal models of non-alcoholic steatohepatitis: of mice and man. Digestive diseases (Basel, Switzerland) 28(1):247–254. https://doi.org/10.1159/000282097
14. Adams LA, Angulo P (2006) Treatment of non-alcoholic fatty liver disease. Postgrad Med J 82(967):315–322. https://doi.org/10.1136/pgmj.2005.042200
15. Machado MV, Michelotti GA, Xie G et al (2015) Mouse models of diet-induced nonalcoholic steatohepatitis reproduce the heterogeneity of the human disease. PLoS ONE 10(5):e0127991. https://doi.org/10.1371/journal.pone.0127991
16. Kanuri G, Bergheim I (2013) In vitro and in vivo models of non-alcoholic fatty liver disease (NAFLD). Int J Mol Sci 14(6):11963–11980. https://doi.org/10.3390/ijms140611963
17. Kozyra M, Johansson I, Nordling Å et al (2018) Human hepatic 3D spheroids as a model for steatosis and insulin resistance. Sci Rep 8(1):14297. https://doi.org/10.1038/s41598-018-32722-6
18. Cole BK, Feaver RE, Wamhoff BR et al (2018) Non-alcoholic fatty liver disease (NAFLD) models in drug discovery. Expert Opin Drug Discov 13(2):193–205. https://doi.org/10.1080/17460441.2018.1410135
19. Hassan S, Sebastian S, Maharjan S et al (2020) Liver-on-a-chip models of fatty liver disease. Hepatology 71(2):733–740. https://doi.org/10.1002/hep.31106
20. Gori M, Simonelli MC, Giannitelli SM et al (2016) Investigating nonalcoholic fatty liver disease in a liver-on-a-chip microfluidic device. PLoS ONE 11(7):e0159729. https://doi.org/10.1371/journal.pone.0159729
21. Ma L, Wu Y, Li Y et al (2020) Current advances on 3D-bioprinted liver tissue models. Adv Healthc Mater 9(24):2001517. https://doi.org/10.1002/adhm.202001517
22. Sacchi M, Bansal R, Rouwkema J (2020) Bioengineered 3D models to recapitulate tissue fibrosis. Trends Biotechnol 38(6):623–636. https://doi.org/10.1016/j.tibtech.2019.12.010
23. Leite SB, Roosens T, El Taghdouini A et al (2016) Novel human hepatic organoid model enables testing of drug-induced liver fibrosis in vitro. Biomaterials 78:1–10. https://doi.org/10.1016/j.biomaterials.2015.11.026
24. Norona LM, Nguyen DG, Gerber DA et al (2016) Editor's highlight: modeling compound-induced fibrogenesis in vitro using three-dimensional bioprinted human liver tissues. Toxicol Sci 154(2):354–367. https://doi.org/10.1093/TOXSCI/KFW169
25. Norona LM, Nguyen DG, Gerber DA et al (2019) Bioprinted liver provides early insight into the role of Kupffer cells in TGF-β1 and methotrexate-induced fibrogenesis. PLoS ONE 14(1):e0208958. https://doi.org/10.1371/journal.pone.0208958
26. Kang K, Kim Y, Jeon H et al (2018) Three-dimensional bioprinting of hepatic structures with directly converted hepatocyte-like cells. Tissue Eng A 24(7–8):576–583. https://doi.org/10.1089/ten.tea.2017.0161
27. Moroni L, Burdick JA, Highley C et al (2018) Biofabrication strategies for 3D in vitro models and regenerative medicine. Nat Rev Mater 3(5):21–37. https://doi.org/10.1038/s41578-018-0006-y
28. Ma X, Qu X, Zhu W et al (2016) Deterministically patterned biomimetic human iPSC-derived hepatic model via rapid 3D bioprinting. Proc Natl Acad Sci USA 113(8):2206–2211. https://doi.org/10.1073/pnas.1524510113
29. Mao Q, Wang Y, Li Y et al (2020) Fabrication of liver microtissue with liver decellularized extracellular matrix (dECM) bioink by digital light processing (DLP) bioprinting. Mater Sci Eng C 109:110625. https://doi.org/10.1016/j.msec.2020.110625
30. Ivanov VV, Decker C (2001) Kinetic study of photoinitiated frontal polymerization. Polym Int 50(1):113–118. https://doi.org/10.1002/1097-0126(200101)50:1<113::AID-PI594>3.0.CO;2-X
31. Knight E, Przyborski S (2015) Advances in 3D cell culture technologies enabling tissue-like structures to be created in vitro. J Anat 227(6):746–756. https://doi.org/10.1111/joa.12257
32. Tsang VL, Chen AA, Cho LM et al (2007) Fabrication of 3D hepatic tissues by additive photopatterning of cellular hydrogels. Faseb J 21(3):790–801. https://doi.org/10.1096/fj.06-7117com
33. Aubin H, Nichol JW, Hutson CB et al (2010) Directed 3D cell alignment and elongation in microengineered hydrogels.

Biomaterials 31(27):6941–6951. https://doi.org/10.1016/j.biomaterials.2010.05.056
34. Hahn MS, Miller JS, West JL (2006) Three-dimensional biochemical and biomechanical patterning of hydrogels for guiding cell behavior. Adv Mater 18(20):2679–2684. https://doi.org/10.1002/adma.200600647
35. Bajaj P, Marchwiany D, Duarte C et al (2013) Patterned three-dimensional encapsulation of embryonic stem cells using dielectrophoresis and stereolithography. Adv Healthc Mater 2(3):450–458. https://doi.org/10.1002/adhm.201200318
36. Pi Q, Maharjan S, Yan X et al (2018) Digitally tunable microfluidic bioprinting of multilayered cannular tissues. Adv Mater 30(43):e1706913. https://doi.org/10.1002/adma.201706913
37. Ying GL, Jiang N, Maharjan S et al (2018) Aqueous two-phase emulsion bioink-enabled 3D bioprinting of porous hydrogels. Adv Mater 30(50):e1805460. https://doi.org/10.1002/adma.201805460
38. Gong J, Schuurmans CC, van Genderen AM et al (2020) Complexation-induced resolution enhancement of 3D-printed hydrogel constructs. Nat Commun 11(1):1267. https://doi.org/10.1038/s41467-020-14997-4
39. Yue K, Li X, Schrobback K et al (2017) Structural analysis of photocrosslinkable methacryloyl-modified protein derivatives. Biomaterials 139:163–171. https://doi.org/10.1016/j.biomaterials.2017.04.050
40. Xu L, Hui AY, Albanis E et al (2005) Human hepatic stellate cell lines, LX-1 and LX-2: new tools for analysis of hepatic fibrosis. Gut 54(1):142–151. https://doi.org/10.1136/gut.2004.042127
41. Štampar M, Frandsen HS, Rogowska-Wrzesinska A et al (2020) Hepatocellular carcinoma (HepG2/C3A) cell-based 3D model for genotoxicity testing of chemicals. Sci Total Environ 755(2):143255. https://doi.org/10.1016/j.scitotenv.2020.143255
42. Ramaiahgari SC, Den Braver MW, Herpers B et al (2014) A 3D in vitro model of differentiated HepG2 cell spheroids with improved liver-like properties for repeated dose high-throughput toxicity studies. Arch Toxicol 88(5):1083–1095. https://doi.org/10.1007/s00204-014-1215-9
43. Seo W, Jeong W-I (2016) Hepatic non-parenchymal cells: master regulators of alcoholic liver disease? World J Gastroenterol 22(4):1348–1356. https://doi.org/10.3748/wjg.v22.i4.1348
44. Friedman SL (2008) Hepatic stellate cells: protean, multifunctional, and enigmatic cells of the liver. Physiol Rev 88(1):125–172. https://doi.org/10.1152/physrev.00013.2007
45. Prestigiacomo V, Weston A, Messner S et al (2017) Pro-fibrotic compounds induce stellate cell activation, ECM-remodelling and Nrf2 activation in a human 3D-multicellular model of liver fibrosis. PLoS ONE 12(6):e0179995. https://doi.org/10.1371/journal.pone.0179995
46. Baze A, Parmentier C, Hendriks DFG et al (2018) Three-dimensional spheroid primary human hepatocytes in monoculture and coculture with nonparenchymal cells. Tissue Eng C Methods 24(9):534–545. https://doi.org/10.1089/ten.tec.2018.0134
47. Loessner D, Meinert C, Kaemmerer E et al (2016) Functionalization, preparation and use of cell-laden gelatin methacryloyl-based hydrogels as modular tissue culture platforms. Nat Protoc 11(4):727–746. https://doi.org/10.1038/nprot.2016.037
48. Klotz BJ, Gawlitta D, Rosenberg A et al (2016) Gelatin-methacryloyl hydrogels: towards biofabrication-based tissue repair. Trends Biotechnol 34(5):394–407. https://doi.org/10.1016/j.tibtech.2016.01.002
49. Ying G, Jiang N, Yu C et al (2018) Three-dimensional bioprinting of gelatin methacryloyl (GelMA). Bio-des Manuf 1(4):215–224. https://doi.org/10.1007/s42242-018-0028-82
50. Hoch E, Schuh C, Hirth T et al (2012) Stiff gelatin hydrogels can be photo-chemically synthesized from low viscous gelatin solutions using molecularly functionalized gelatin with a high degree of methacrylation. J Mater Sci Mater Med 23(11):2607–2617. https://doi.org/10.1007/s10856-012-4731-2
51. Senoo H (2004) Structure and function of hepatic stellate cells. Med Electron Microsc 37(1):3–15. https://doi.org/10.1007/s00795-003-0230-3
52. Fausto N, Campbell JS (2003) The role of hepatocytes and oval cells in liver regeneration and repopulation. Mech Dev 120(1):117–130. https://doi.org/10.1016/S0925-4773(02)00338-6
53. Tsuchida T, Friedman SL (2017) Mechanisms of hepatic stellate cell activation. Nat Rev Gastroenterol Hepatol 14(7):397–411. https://doi.org/10.1038/nrgastro.2017.38
54. Washington K, Wright K, Shyr Y et al (2000) Hepatic stellate cell activation in nonalcoholic steatohepatitis and fatty liver. Hum Pathol 31(7):822–828. https://doi.org/10.1053/hupa.2000.8440
55. Takahara I, Akazawa Y, Tabuchi M et al (2017) Toyocamycin attenuates free fatty acid-induced hepatic steatosis and apoptosis in cultured hepatocytes and ameliorates nonalcoholic fatty liver disease in mice. PLoS ONE 12(3):e0170591. https://doi.org/10.1371/journal.pone.0170591
56. Jung IR, Choi SE, Hong SA et al (2017) Sodium fluorocitrate having protective effect on palmitate-induced beta cell death improves hyperglycemia in diabetic db/db mice. Sci Rep 7(1):12916. https://doi.org/10.1038/s41598-017-13365-5
57. Friedman SL (2010) Evolving challenges in hepatic fibrosis. Nat Rev Gastroenterol Hepatol 7(8):425–436. https://doi.org/10.1038/nrgastro.2010.97
58. Mederacke I, Hsu CC, Troeger JS et al (2013) Fate tracing reveals hepatic stellate cells as dominant contributors to liver fibrosis independent of its aetiology. Nat Commun 4:2823. https://doi.org/10.1038/ncomms3823
59. Gressner AM, Weiskirchen R, Breitkopf K et al (2002) Roles of TGF-beta in hepatic fibrosis. Front Biosci 7:d793–d807. PMID: 11897555. https://pubmed.ncbi.nlm.nih.gov/11897555/
60. Yang L, Roh YS, Song J et al (2014) Transforming growth factor beta signaling in hepatocytes participates in steatohepatitis through regulation of cell death and lipid metabolism in mice. Hepatology 59(2):483–495. https://doi.org/10.1002/hep.26698
61. Kim YJ, Lee ES, Kim SH et al (2014) Inhibitory effects of rapamycin on the different stages of hepatic fibrosis. World J Gastroenterol 20(23):7452–7460. https://doi.org/10.3748/wjg.v20.i23.7452
62. Saadati S, Sadeghi A, Mansour A et al (2019) Curcumin and inflammation in non-alcoholic fatty liver disease: a randomized, placebo controlled clinical trial. BMC Gastroenterol 19(1):133. https://doi.org/10.1186/s12876-019-1055-4
63. Farzaei MH, Zobeiri M, Parvizi F et al (2018) Curcumin in liver diseases: a systematic review of the cellular mechanisms of oxidative stress and clinical perspective. Nutrients 10(7):855. https://doi.org/10.3390/nu10070855
64. Arab JP, Arrese M, Trauner M (2018) Recent insights into the pathogenesis of nonalcoholic fatty liver disease. Annu Rev Pathol 13:321–350. https://doi.org/10.1146/annurev-pathol-020117-043617